

# Gravitational Plane Waves in Anti-de Sitter Space-Time

Jack Zidich (71736657)

February 11, 2022

# Chapter 1

## Introduction

The aim of this project was to determine how gravitational waves propagate in AdS space-time, and to explore particular effects, such as collisions, using a numerical simulation based on the Python package COFFEE. Only the specific case of plane-symmetric gravitational waves travelling through a vacuum (ie. without matter) was considered. How geometric scalars such as  $\rho$  and  $\sigma$ , as defined in section 1.2, vary in simulations, both with and without waves, and in linear and non-linear regimes, was explored so as to get a picture of the geometry of AdS., convergence tests on the constraint variables were employed to verify the validity of the simulation results.

# Chapter 2

## Background

### 2.1 Anti-de Sitter space-time

Anti-de Sitter (AdS) space-time is a space-time which has a negative cosmological constant ( $\lambda < 0$ ), in contrast to de Sitter space-time which has a positive cosmological constant ( $\lambda > 0$ ) and Minkowski space which has a zero cosmological constant ( $\lambda = 0$ ). For the purposes of this report, the cosmological constant will be taken to refer to  $\Lambda$ , where  $\Lambda = \frac{\lambda}{6}$  (Penrose & Rindler, 1986). AdS is derived from the hyperboloid  $-u^2 - v^2 + x^2 + y^2 + z^2 = \frac{1}{H^2}$ , where H is the Hubble constant and is related to the cosmological constant  $\Lambda$  by  $H^2 = -2\Lambda$  in the case of AdS, embedded in a flat 5-dimensional space with metric  $ds^2 = -du^2 - dv^2 + dx^2 + dy^2 + dz^2$  (Bengtsson, 1998). From this, Hawking & Ellis (1973) derived the metric  $ds^2 = -cosh^2(r)dt^2 + dr^2 + sinh^2(r)(d\theta^2 + sin^2(\theta)d\phi^2)$  for AdS, which, with a change of coordinates to be more appropriate for a plane-symmetric application, is equivalent to  $ds^2 = e^{-2Hz}(dt^2 - dx^2 - dy^2) - dz^2$ . Transforming this in turn to the co-moving coordinates  $t \rightarrow te^{zH}$  gives equation 2.1, the metric used for this project.

$$ds^2 = dt^2 + 2Htdtdz - e^{-2Hz}(dx^2 + dy^2) + ((Ht)^2 - 1)dz^2 \quad (2.1)$$

### 2.2 Gravitational waves

Gravitational waves are propagating perturbations in the curvature of space-time, which travel at the speed of light. In this report only plane-symmetric gravitational waves will be considered, a restriction that notably is non-physical since any finite source of gravitational radiation will only produce curved wave-fronts (Griffiths, 2016), however, it substantially simplifies the scenario which is why it is still beneficial to consider as a base case. Plane-symmetric gravitational waves are defined as those which only vary in two dimensions, z and t, and not in the other two dimensions, x and y. Hence the waves can be fully visualized on a one-dimensional line, changing step-by-step in time, or on a contour plot, with all z and t positions shown on a single graph with colour used to indicate magnitude, both of which will be used to illustrate the results of this project.

### 2.3 Friedrich-Nagy gauge

To be able to simulate general relativity in infinite physical systems, it is necessary to impose a non-physical boundary to the system. The difficulty, however, in doing so is ensuring the problem is well-posed at the boundary, resulting in an initial boundary value problem (IBVP). One approach to solving this IBVP, as presented by Friedrich & Nagy (1999) involves formulating the Einstein field equations as a system of first-order partial differential equations involving various geometrical scalar parameters, along with a set of boundary conditions, termed the Friedrich-Nagy gauge, which ensures the problem is well-posed. This approach, which differs from the standard numerical solutions by being first-order rather than second-order, was first implemented numerically by Frauendiener & Stevens (2014), and it is the program they developed which was used for this project. Notably, the only boundary conditions required by their system are for the Weyl tensor components  $\psi_0$  and  $\psi_4$  at the right and left boundaries respectively.

## 2.4 Newman-Penrose formalism

The equations required for this numerical simulation were derived using the Newman-Penrose formalism (Newman & Penrose, 1962). On this approach, once plane-symmetry is taken into consideration, the two remaining null-directions along which waves can propagate from each point in the plane are termed  $n$  (ingoing waves) and  $l$  (outgoing waves), and are both orthogonal to the plane and normalised such that  $l^a n_a = 0$  (Frauendiener & Stevens, 2014). The equations for these are given in equations 2.2 and 2.3.

$$n^a = \frac{(1 - B)\partial_t^a - A\partial_z^a}{\sqrt{2}} \quad (2.2)$$

$$l^a = \frac{(1 + B)\partial_t^a + A\partial_z^a}{\sqrt{2}} \quad (2.3)$$

The form of the metric with these conditions taken into account is given in equation 2.4 (Frauendiener et al., 2021), where  $A$ ,  $B$ ,  $\xi$  and  $\eta$  are invariant functions of  $z$  and  $t$ .

$$g = dt^2 - \frac{2B}{A}dtdz - \frac{1 - B^2}{A^2}dz^2 + \frac{2}{(\bar{\xi}(\eta) - \bar{\xi}(\xi)\eta)^2}(\eta dx - \xi dy)(\bar{\eta}dx - \bar{\xi}dy) \quad (2.4)$$

By comparing the AdS metric in equation 2.1 with the general form of the Newman-Penrose metric in equation 2.4, it can be seen that  $2Ht = \frac{-2B}{A}$  and  $Ht^2 - 1 = \frac{B^2 - 1}{A^2}$ , which can be solved to give  $B = \pm Ht$  and  $A = \mp 1$ . Since  $A$  is associated with the scale of the  $z$ -direction, it must be taken as positive. This gives equations 2.5 and 2.6 for  $A$  and  $B$ .

$$A = 1 \quad (2.5)$$

$$B = -Ht \quad (2.6)$$

Gravitational waves in this formalism are represented by the Weyl tensor components,  $\psi_i$  for  $i$  between 0 and 4. Due to the restriction of plane symmetry, two of these are zero and a third is fixed by the values of the geometric scalar quantities, with these conditions given by equations 2.7 and 2.8 (Frauendiener et al., 2021). The two remaining components,  $\psi_4$  and  $\psi_0$ , however, are free to vary, and corresponding to waves travelling in the  $n$  and  $l$  directions, from the left and right boundaries, respectively.

$$\psi_1 = \psi_3 = 0 \quad (2.7)$$

$$\psi_2 = \sigma\sigma' - \rho\rho' + \Lambda \quad (2.8)$$

The quantities  $\rho$  and  $\rho'$  here represent a divergence (if negative) or convergence (if positive) in the  $n$  and  $l$  directions respectively, and likewise  $\sigma$  and  $\sigma'$  represent shear. Algebraic conditions on these parameters, and other variables standard to the formalism that are unimportant for this report, due to the conditions imposed, are listed in equations 2.9 through 2.11 below from Frauendiener et al., 2021.

$$\rho = \bar{\rho} \quad (2.9)$$

$$\rho' = \bar{\rho}' \quad (2.10)$$

$$\kappa = \kappa' = \alpha = \beta = \tau = \tau' = 0 \quad (2.11)$$

Due to the further restriction of only considering waves travelling through a vacuum, the Ricci tensor and scalar were both zero, with the Riemann tensor being equal simply to the Weyl tensor. All the components of the Ricci tensor,  $\Phi_{ij}$ , from the Newman-Penrose formalism, are thus zero, as stated in equation 2.12 (Frauendiener et al., 2021).

$$\Phi_{00} = \Phi_{01} = \Phi_{10} = \Phi_{11} = \Phi_{12} = \Phi_{21} = \Phi_{22} = 0 \quad (2.12)$$

Equations 2.13 through 2.21, also listed from Frauendiener et al., 2021, with the additional stipulation of the Ricci tensor components being zero, are evolution equations, used by the numerical simulation to evolve each of the parameters of the system in time. In the case with no matter, these form a closed system of symmetric hyperbolic partial differential equations.

$$\partial_t A = \frac{A(\mu + \bar{\mu})}{\sqrt{2}} \quad (2.13)$$

$$\partial_t B = \frac{F + \bar{F} + B(\mu + \bar{\mu}) + 2(\rho - \rho')}{\sqrt{2}} \quad (2.14)$$

$$\partial_t \mu = \frac{-F^2 - 3F\rho + \mu\rho - 3\rho^2 - \sigma\bar{\sigma} - \bar{F}(F + \rho - \rho') + \rho'(3F + \mu + 6\rho - 3\rho') + \mu^2 - 6\Lambda + \bar{\mu}(\mu + \rho + \rho') + 2\sigma\sigma' - \bar{\sigma}'\sigma' - \sqrt{2}B\partial_z(F) - \sqrt{2}A\partial_z(F)}{\sqrt{2}} \quad (2.15)$$

$$\partial_t \rho = \frac{\rho(F + \bar{F} + 3\rho) + \sigma\bar{\sigma} - 3\Lambda}{\sqrt{2}} \quad (2.16)$$

$$\partial_t \rho' = \frac{-\rho'(F + \bar{F} - 3\rho') + \sigma'\bar{\sigma}' - 3\Lambda}{\sqrt{2}} \quad (2.17)$$

$$\partial_t \sigma = \frac{\rho\bar{\sigma}' + \psi_0 - \sigma(3F + \bar{F} + 4\rho + \rho')}{\sqrt{2}} \quad (2.18)$$

$$\partial_t \sigma' = \frac{\rho'\bar{\sigma} + \psi_4 - \sigma'(-3F + \bar{F} + 4\rho' - \rho)}{\sqrt{2}} \quad (2.19)$$

$$\partial_t \psi_0 = \frac{-6\sigma\psi_2 + 2\psi_0(-2(F + \mu + \rho) + \rho') - \sqrt{2}A\partial_z(\psi_0)}{(B - 1)\sqrt{2}} \quad (2.20)$$

$$\partial_t \psi_4 = \frac{6\sigma'\psi_2 - 2\psi_4(2(F - \mu - \rho') + \rho) - \sqrt{2}A\partial_z(\psi_4)}{(B + 1)\sqrt{2}} \quad (2.21)$$

Additionally, the simulation used evolution equations for  $u$ ,  $v$ ,  $\eta$ , and  $\xi$ , given in equations 2.22 through 2.25 below. These are, however, independent of the above evolution equations, and the latter two quantities were not significant for this project.

$$\partial_t u = \frac{-A\partial_z(u)}{1 + B} \quad (2.22)$$

$$\partial_t v = \frac{A\partial_z(v)}{1 - B} \quad (2.23)$$

$$\partial_t \eta = \frac{\eta(F - \bar{F} + \rho + \rho') + \bar{\eta}(\sigma + \bar{\sigma}')}{\sqrt{2}} \quad (2.24)$$

$$\partial_t \xi = \frac{\xi(F - \bar{F} + \rho + \rho') + \bar{\xi}(\sigma + \bar{\sigma}')}{\sqrt{2}} \quad (2.25)$$

Equations 2.26 through 2.29 are a system of linear ordinary differential equations of four constraint quantities, as listed by Frauendiener et al., 2021, that are necessarily satisfied for the system, assuming appropriate initial conditions are used. Since, however, the simulation does not directly take these equations into account in its evolution and only a finite grid of points is used, these equalities will not be precisely satisfied. For the simulation to be valid, the error of these constraints must tend towards zero at the right order as the number of grid points becomes large. To confirm this, a convergence test must be used, as is done in section 4.6.

$$C_1 = \sqrt{2}A\partial_z(\rho) - (1 - 3B)\rho^2 - (1 - B)\sigma\bar{\sigma} + \rho(\mu + \bar{\mu} + 2\rho') + \rho B(F + \bar{F}) - 3(1 + B)\Lambda = 0 \quad (2.26)$$

$$C_2 = \sqrt{2}A\partial_z(\rho') + (1 + 3B)\rho'^2 + (1 + B)\sigma'\bar{\sigma}' - \rho'(\mu + \bar{\mu} + 2\rho) - \rho'B(F + \bar{F}) + 3(1 - B)\Lambda = 0 \quad (2.27)$$

$$C_3 = \sqrt{2}A\partial_z(\sigma) + (1 + B)\rho\bar{\sigma}' - 2(1 - 2B)\sigma\rho + \sigma(3\mu - \bar{\mu}) + (1 - B)\rho'\sigma + \sigma B(3F - \bar{F}) - (1 - B)\psi_0 = 0 \quad (2.28)$$

$$C_4 = \sqrt{2}A\partial_z(\sigma') - (1 - B)\rho'\bar{\sigma} + 2(1 + 2B)\sigma'\rho' - \sigma'(3\mu - \bar{\mu}) - (1 + B)\rho\sigma' - \sigma'B'(3F - \bar{F}) + (1 + B)\psi_4 = 0 \quad (2.29)$$

Two further derived quantities are used in this report:  $I$ , the Weyl scalar curvature invariant, and  $H$ , a measure of the space-time's expansion rate, proportional to the mean extrinsic curvature. The definitions of these are given in 2.30 and 2.31, again from Frauendiener et al., 2021.

$$I = 2\psi_0\psi_4 + 6\psi_2^2 \quad (2.30)$$

$$H = \frac{\sqrt{2}(B^2 - 1)(B(F + \bar{F}) + \mu + \bar{\mu} + 2(\rho + \rho')) - 2A\partial_z(B)}{6(1 - B^2)^{3/2}} \quad (2.31)$$

## 2.5 Null coordinates

The general equations which the null coordinates,  $u$  and  $v$ , with the values for  $l^a$  and  $n^a$  substituted in from equations 2.2 and 2.3, must satisfy are given in equations 2.32 and 2.33.

$$l^a \nabla_a(u) = (1 + B)\partial_t(u) + A\partial_z(u) = 0 \quad (2.32)$$

$$n^a \nabla_a(v) = (1 - B)\partial_t(v) - A\partial_z(v) = 0 \quad (2.33)$$

Substituting 2.5 and 2.6 for  $A$  and  $B$  into the above gives the partial differential equations  $(1 - Ht)\partial_t u + \partial_z(u) = 0$  and  $(1 + Ht)\partial_t(v) - \partial_z(v) = 0$ , which can be solved using the method of characteristics to get the general solutions  $u(t, z) = f((t - \frac{1}{H})e^{Hz} + \frac{1}{H})$  and  $v(t, z) = g((t + \frac{1}{H})e^{Hz} - \frac{1}{H})$ . Taking the boundaries for the simulations to be  $z = -1$  and  $z = 1$  these become  $u(t, -1) = f((t - \frac{1}{H})e^{-H} + \frac{1}{H})$  and  $v(t, 1) = g((t + \frac{1}{H})e^H - \frac{1}{H})$ . Since  $f$  and  $g$  are arbitrary functions, and  $H$  is a constant, functions  $f$  and  $g$  can be chosen to satisfy equations 2.34 and 2.35, which was the choice of boundary values for the null coordinates used in this project.

$$u(t, -1) = \frac{t}{\sqrt{2}} \quad (2.34)$$

$$v(t, 1) = \frac{t}{\sqrt{2}} \quad (2.35)$$

## 2.6 Geodesics

For a geodesic in the situation considered, all velocities are zero except for the  $t$ -velocity. Framing the geodesic equation,  $\ddot{x}^i + \Gamma_{jk}^i \dot{x}^j \dot{x}^k$ , where dotted variables represent differentiation with respect to a dummy variable  $\lambda$ , for  $t$  gives the ordinary differential equation  $\ddot{t} + \Gamma_{00}^0 t^2$ , using the metric from equation 2.1 and noting that all other terms are zero here. This equation can be solved to give  $t(\lambda) = \frac{\sqrt{2}}{H} \text{erfi}^{-1}(Hc_1(\lambda + c_2))$ . With the condition  $t(0) = 0$  this gives  $Hc_1c_2 = 0$ , and since  $H \neq 0$  and since if  $c_1 = 0$  then  $t(\lambda) = 0$  for all  $\lambda$ , it follows that  $c_2 = 0$ . The resulting geodesic is then given in equation 2.36, where  $c_1$  is left as an arbitrary real constant. In this equation,  $\text{erfi}^{-1}$  is the inverse imaginary error function, defined as the inverse of the imaginary error function  $\text{erfi}(x) = \frac{2}{\sqrt{\pi}} \int_0^x e^{t^2} dt$ . This function maps the reals onto the reals, and so the geodesic covers all real  $t$  values.

$$t(\lambda) = \frac{\sqrt{2}}{H} \text{erfi}^{-1}(Hc_1\lambda) \quad (2.36)$$

## 2.7 AdS/CFT correspondence

There has been substantial interest in anti-de Sitter space-times since 1997, when Maldacena published a conjecture known as the AdS/CFT correspondence, which proposed an equivalence between two frameworks for describing a particular black hole system - the first, a string theory approach which views the geometry near the event horizon of a black hole as the product of anti-de Sitter space-time and a sphere, and a quantum field theory approach, which views it as a conformal field theory in fewer dimensions. This correspondence between gravity and gauge theories has since been generalised and greatly expanded upon, and has found applications by allowing for the simplification of problems involving certain kinds of quantum systems by reference to general relativity (Hubeny, 2015). It is beyond the scope of this report to discuss this correspondence further, however, the findings regarding the geometry of AdS could potentially be of value for further research in this field.

# Chapter 3

## Method

### 3.1 COFFEE

This project used the Python package COFFEE (Doulis et al., 2019) to numerically simulate the evolution of the AdS system. This package is designed to solve a time-dependent system of partial differential equations, such as is necessary for the study of general relativity, using the method of lines, balancing a desire for both speed (accomplished via MPI parallelisation) and usability (accomplished via being written in Python and allowing for substantial flexibility). For the purposes of this project, the solver used was an implementation of a fourth order Runge-Kutta method and the summation by parts finite difference operator used was D43 Strand (Strand, 1994) using the simultaneous approximation method, as introduced by Carpenter et al. (1994), to apply stable boundary conditions.

### 3.2 Initial conditions

The initial conditions (the same at all z-positions), excluding those stated in section 2, used as parameters in all AdS simulations are given in equations 3.1 through 3.3.

$$\rho = \sqrt{-\Lambda} \tag{3.1}$$

$$\rho' = -\sqrt{-\Lambda} \tag{3.2}$$

$$\sigma = \sigma' = \mu = H = I = \psi_0 = \psi_4 = 0 \tag{3.3}$$

Two different values for the remaining gauge variable, F, were tried for this project: the exact gauge, which reproduces the exact AdS metric used and so will be the focus in the results section of this report, and the Gauß gauge. The exact gauge is defined here by setting  $F = \bar{F} = -3\sqrt{-\Lambda}$  for all t and z values, whereas the Gauß gauge is defined by having the same initial condition but varying F such that  $dB/dt = 0$ . The exact parameters used for running the simulation varied between tests but, except where otherwise stated, the number of grid points used was 1600 and the CFL used was 1.5.

### 3.3 Waves

For simulations with a wave or waves, the main cases tested were those using a smoothed sinusoidal wave  $32\sin(\frac{35\pi t}{4})^8$ , or variations on this, as the boundary condition for  $\psi_0$  or  $\psi_4$ . For most such cases, only a single period of such a wave was used, ie. this formula was used from the start of the simulation until  $t = \frac{435}{35}$ , after which the boundary condition was indefinitely zero. Such a wave has an amplitude of 1, an area of 1, and a maximum  $\psi$  value of 32.

### 3.4 Linearization

To discern which effects are linear and which non-linear, linearized versions of the evolution equations were derived by substituting  $X = X_0 + \epsilon X_1$  for each variable  $X$  into these equations and solving for  $X_1$ , discarding terms

non-linear in  $\epsilon$  and  $X_0$  that are zero in all cases with the exact gauge. The resulting linearized evolution equations are given in equations 3.1 through 3.13.

$$\partial_t A = \frac{A_0(\mu + \bar{\mu})}{\sqrt{2}} \quad (3.4)$$

$$\partial_t B = \frac{F_0 + \bar{F}_0 + 2\rho - 2\rho'}{\sqrt{2}} \quad (3.5)$$

$$\partial_t \mu = \frac{\rho_0(\mu + m\bar{u} - 6\rho) + \bar{F}_0(-\rho + \rho') + \rho'(3F_0 + 6\rho_0 - 6\rho'_0) + \rho'_0(\bar{\mu} + \mu + 6\rho) - 3F_0\rho}{\sqrt{2}} \quad (3.6)$$

$$\partial_t \rho = \frac{\rho(F_0 + \bar{F}_0 + 6\rho_0)}{\sqrt{2}} \quad (3.7)$$

$$\partial_t \rho' = \frac{-\rho'(F_0 + \bar{F}_0 - 6\rho'_0))}{\sqrt{2}} \quad (3.8)$$

$$\partial_t \sigma = \frac{\sigma(3F_0 + 4\rho_0 - \bar{F}_0 - \rho'_0) + \bar{\sigma}'\rho_0 + \psi_0}{\sqrt{2}} \quad (3.9)$$

$$\partial_t \sigma' = \frac{\sigma'(-3F_0 + 4\rho'_0 + \bar{F}_0 - \rho_0) + \bar{\sigma}\rho'_0 + \psi_4}{\sqrt{2}} \quad (3.10)$$

$$\partial_t \psi_0 = \frac{A_0 \partial_z(\psi_0) - \psi_0(4F_0 + 4\rho_0 - 2\rho'_0)}{-\sqrt{2}} \quad (3.11)$$

$$\partial_t \psi_4 = \frac{A_0 \partial_z(\psi_4) - \psi_4(4F_0 - 4\rho'_0 + 2\rho_0)}{\sqrt{2}} \quad (3.12)$$

$$\partial_t \eta = \frac{\eta(F_0 - \bar{F}_0 + \rho_0 + \rho'_0) + \eta_0(\rho + \rho') + \bar{\eta}_0(\sigma + \bar{\sigma}')}{\sqrt{2}} \quad (3.13)$$

$$\partial_t \xi = \frac{\xi(F_0 - \bar{F}_0 + \rho_0 + \rho'_0) + \xi_0(\rho + \rho') + \bar{\xi}_0(\sigma + \bar{\sigma}')}{\sqrt{2}} \quad (3.14)$$

$$\partial_t u = -A_0 \partial_z(u) - A \partial_z(u_0) \quad (3.15)$$

$$\partial_t v = A_0 \partial_z(v) + A \partial_z(v_0) \quad (3.16)$$

# Chapter 4

## Results

### 4.1 AdS space-time with no waves

The first simulations made were of AdS space-time with no waves. The initial conditions, as described in section 3.2, are graphically displayed in Figure 4.1. In the exact gauge,  $H$  decreases uniformly over time, whereas the other variables remain constant. In the Gauß gauge,  $H$  still decreases uniformly, but  $\rho$ ,  $\rho'$  and  $\mu$  also increase likewise.

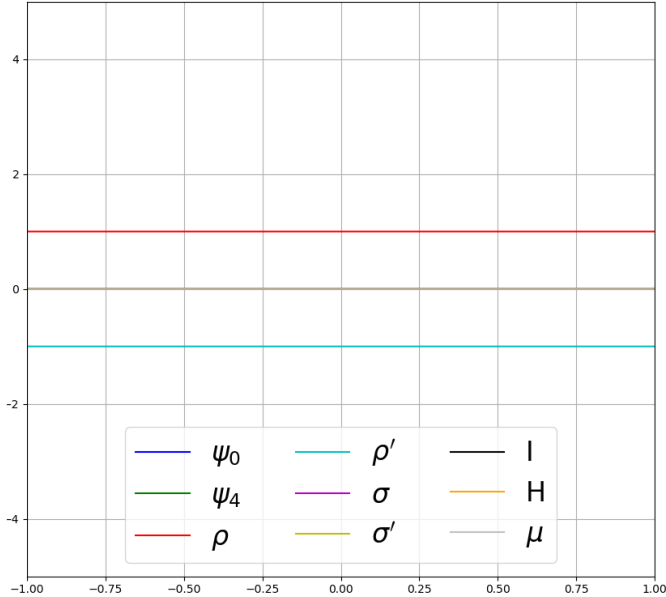
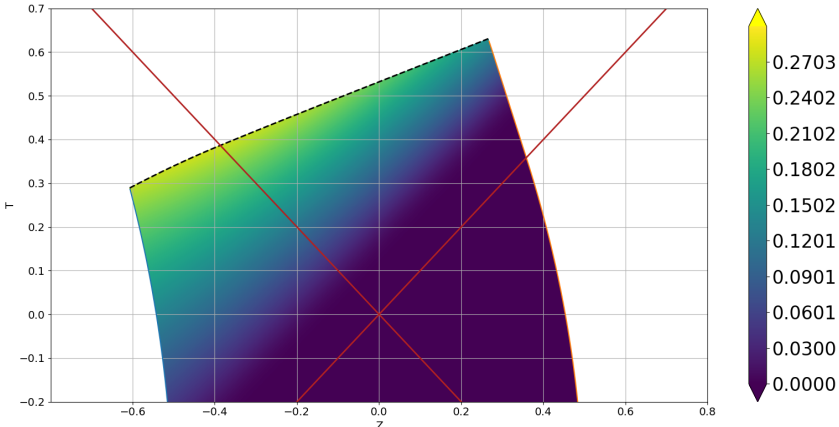


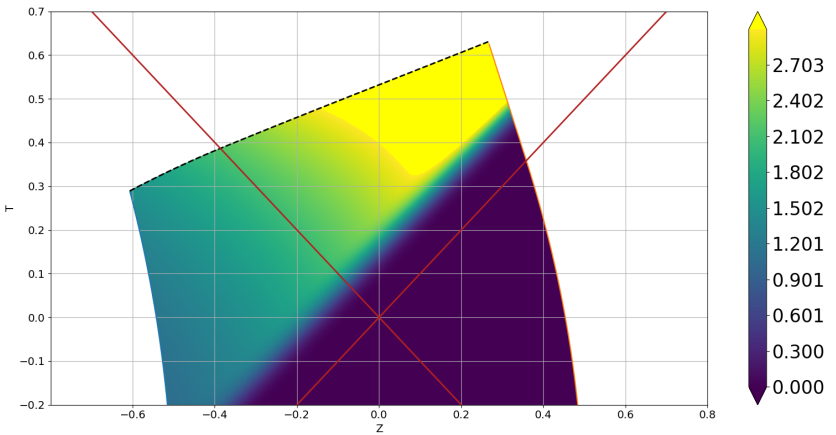
Figure 4.1: Initial conditions of the simulation with a cosmological constant of -1

### 4.2 Positive $\psi_4$ wave

Considering first the exact gauge with a single-period positive wave for the  $\psi_4$  variable: as the wave passes,  $\sigma'$  increases to a value equal to the area of the wave (initially 1) and, after the wave has passed,  $\sigma'$  continues to increase gradually, as do  $\sigma$  and  $\rho'$ , whereas  $\mu$  decreases and  $H$  decreases at an increased rate. Contour plots comparing the trends for  $\sigma$  and  $\sigma'$  are shown in Figure 4.2. The rate at which all these variables change after the wave has passed is greater for larger negative values of the cosmological constant. The amplitude of the  $\psi_4$  wave also increases as it travels, with the rate of increase proportional to  $\rho$ , which is larger for larger negative cosmological constants. All these effects are identical to what is observed with a positive cosmological constant of equal magnitude.



(a)  $\sigma$



(b)  $\sigma'$

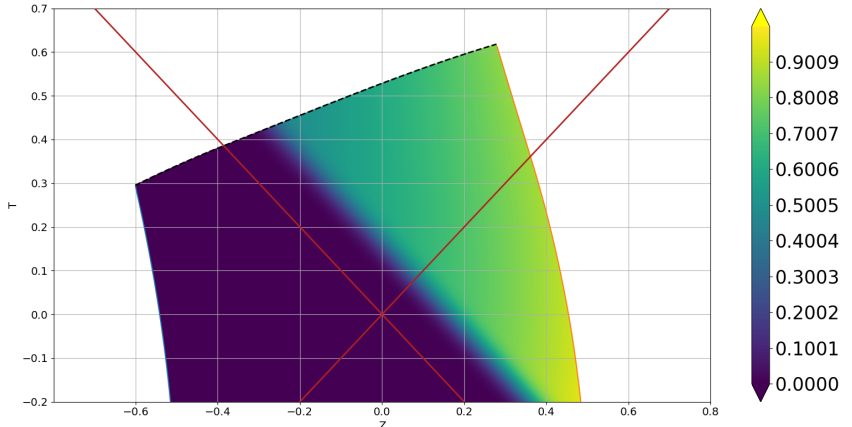
Figure 4.2: Contour plots for a single-peak positive  $\psi_4$  wave with a cosmological constant of -1. Note that the scales for the two graphs are different.

### 4.3 Positive $\psi_0$ wave

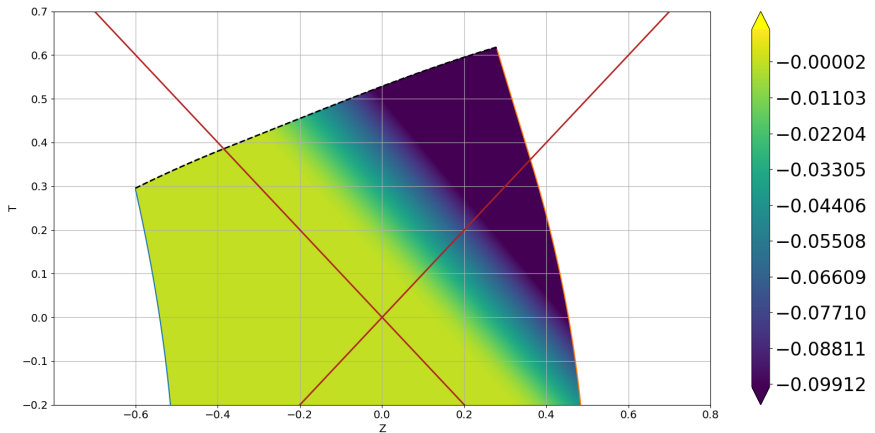
With an equivalent wave to the above but in the  $\psi_0$  direction, the effects are similar, except that it is  $\sigma$  that increases as the wave passes, not  $\sigma'$ , and after the wave has passed,  $\sigma'$  decreases rather than increases and  $\rho$  increases, rather than  $\rho'$ . Contour plots for  $\sigma$  and  $\sigma'$  are shown in Figure 4.3 which can be compared to those in 4.2 for a  $\psi_4$  wave. The wave also decreases as it travels, since the rate of change is proportional to  $\rho'$ , which starts negative, rather than the positive  $\rho$  variable as in the psi4 case. This is unlike with a positive cosmological constant, where  $\rho$  and  $\rho'$  both start positive and equal, rather than equal but opposite in sign, in which case the psi0 wave increases just as the psi4 one does. Figure 4.4 compares  $\psi_0$ , from this case, and  $\psi_4$ , from the case in section 4.2, to show how they grow and shrink in magnitude as they travel.

### 4.4 Negative waves

Taking the same wave but negative, the effect for a psi4 wave is the same as in the positive case, but with  $\sigma$  and  $\sigma'$  decreasing rather than increasing. This difference between the negative and positive cases here is the same as with a positive cosmological constant. With a positive cosmological constant, the same effect is also seen for a psi0 wave -  $\sigma$  and  $\sigma'$  decrease rather than increase. This is not true, however, in AdS, in which case the negative psi0



(a)  $\sigma$



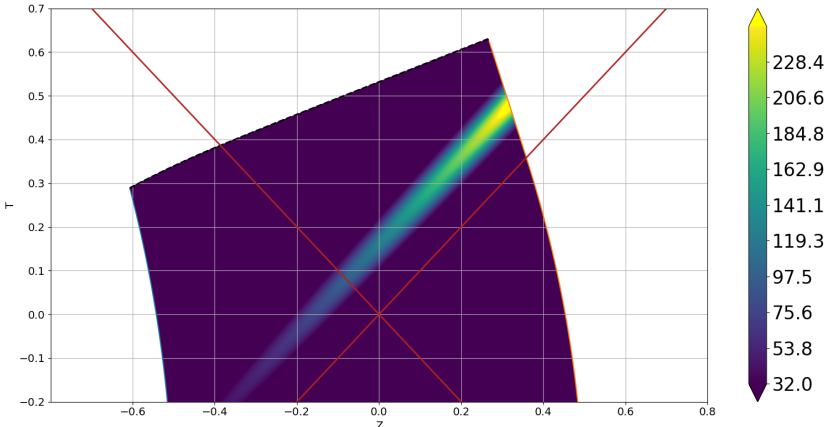
(b)  $\sigma'$

Figure 4.3: Contour plots for a single-peak positive  $\psi_0$  wave with a cosmological constant of -1. Note that the scales for the two graphs are different, and also differ from those in Figure 3.2.

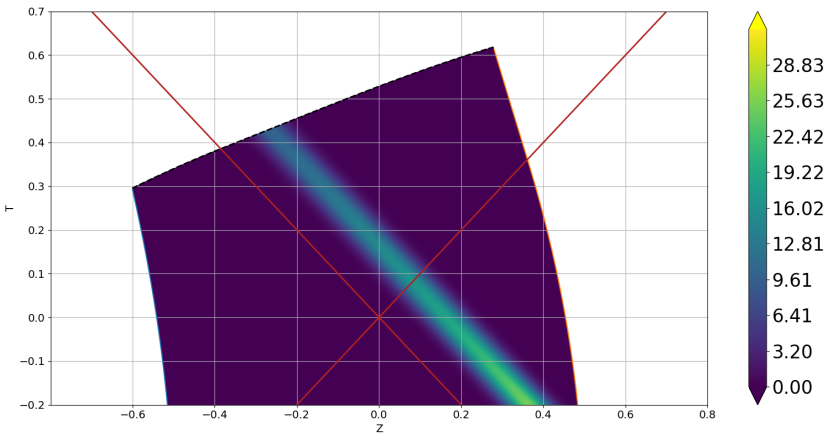
wave causes  $\sigma$  to go negative as it passes, but after that  $\sigma'$  increases and  $\sigma$  either decreases for a small negative cosmological constant (eg. -0.1) or increases for a large negative cosmological constant (eg. -5). It can be seen from the equations for the change of  $\sigma$  over time used by the simulation that the asymmetry between the dS and AdS cases for this variable is a result of  $\rho'$  starting positive in the former but negative in the latter: the dominant term in  $\partial_t \sigma'$  here is  $\bar{\sigma} \rho'$ , which is negative for positive  $\rho'$  (dS) but positive for negative  $\rho'$  (AdS). For  $\partial_t \sigma$  the situation is more complex, since there is no dominant term for all cases, but again the sign of  $\rho'$ , plus that of  $\sigma'$ , is significant.

## 4.5 Collisions

In a collision between a psi4 and psi0 wave, the effect is a large peak in  $I$  during the collision, and after collision for there to a region of positive  $I$  between the two waves, expanding as they travel, with the magnitude at each wave proportional to the amplitude of the wave. If both waves are of the same sign, the peak during collision is positive, whereas it is negative if they of opposite sign, but post-collision  $I$  is positive in all cases. These collision effects are the same as in dS, except that in AdS the shrinking of the psi0 wave and growing of the psi4 wave results in the region of  $I$  post-collision being asymmetrical, whereas in dS it is symmetrical. This can be seen in the contour plots of  $I$  for such a collision in Figure 4.2, with both showing a similar collision peak for  $I$  at  $z = 0$ , but after this



(a) Positive  $\psi_4$  wave



(b) Positive  $\psi_0$  wave

Figure 4.4: Contour plots comparing the changes in the  $\psi$  variables from the cases considered in section 4.2 and 4.3 with a cosmological constant of -1. Note that the scales for the two graphs are different.

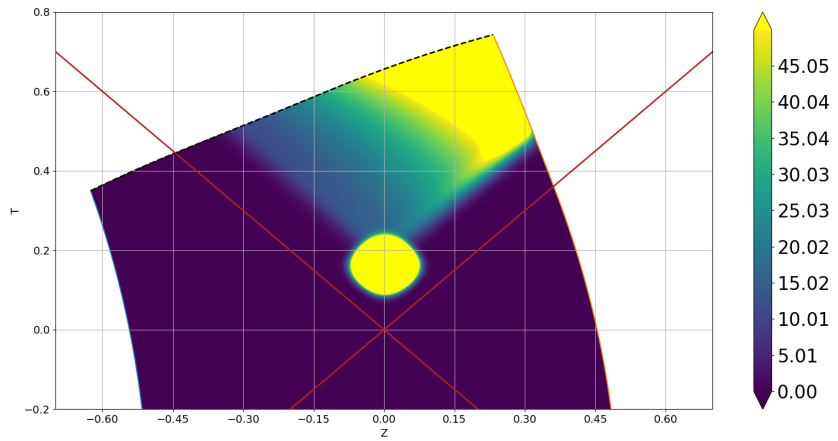
having an asymmetrical increase in  $I$  in the AdS case (4.2a) but a symmetrical one in the dS case (4.2b).

## 4.6 Convergence test

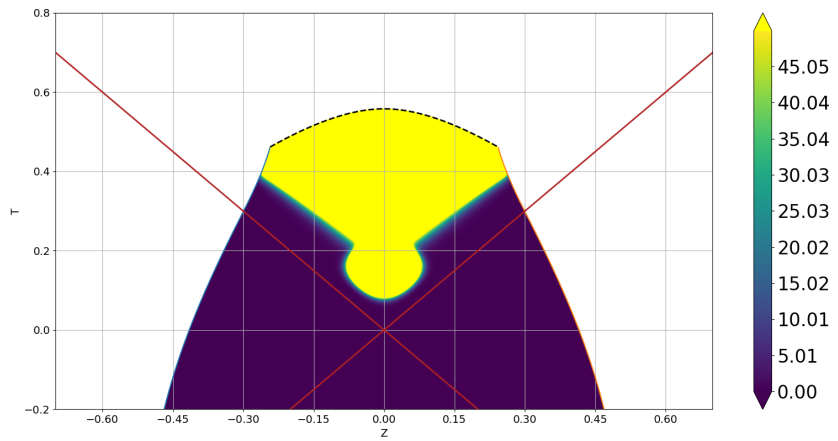
A convergence test for the collision described in the previous section was ran with  $\Lambda = -1$  to ensure that the results of the simulation converge towards satisfying the constraint equations (2.26 through 2.29). This was done by running the simulation with an increasing number of grid points (100, 200, 400, 800, 1600, 3200) and then plotting the magnitudes of the constraint variables at each time step for each case. The resulting graph for  $C_1$  (as defined in equation 2.26) plotted on a logarithmic scale, is shown in Figure 4.3 - it can be seen that the constraint converges as desired towards zero at the correct rate.

## 4.7 Linear evolution

Using the linearized evolution equations (3.4 through 3.16), the simulation gave identical results as with the non-linear equations in the case with no waves - all the variables that remained constant previously were constant with the linearized equations, and  $H$  decreased from 0 at  $t = 0$  to  $-0.22360679774982528$  at  $t = 1$  with  $\Lambda = -0.1$  in



(a)  $\Lambda = -1$



(b)  $\Lambda = 1$

Figure 4.5: Contour plots for  $I$  in the case of the collision of two positive half waves

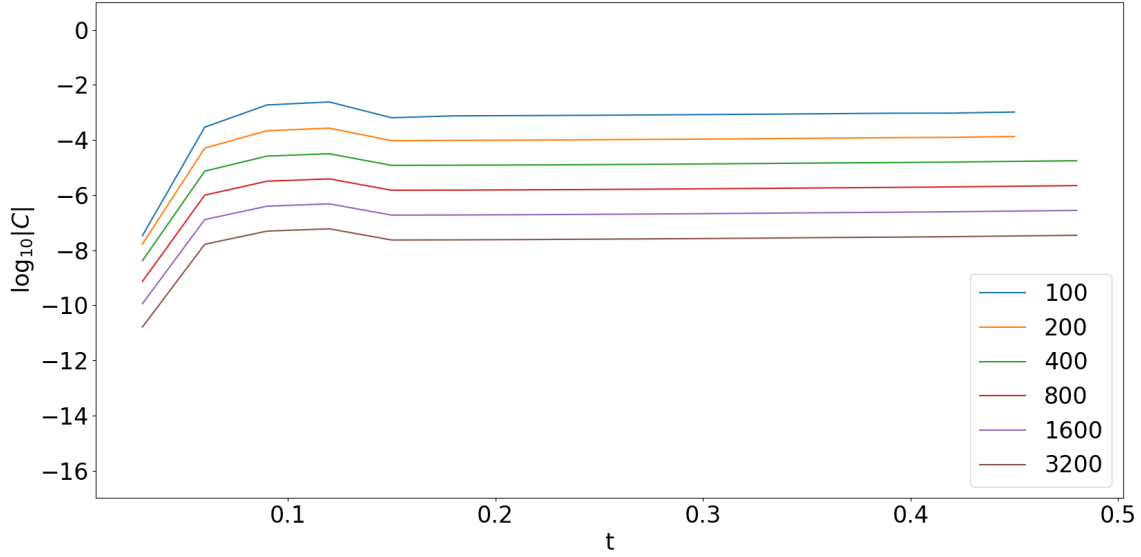


Figure 4.6: Convergence test for the collision of two positive half waves with  $\Lambda = -1$

the linearized case and it decreased to  $-0.2236067977498254$  in the non-linear case during the same time, which is the same result to 15 significant figures. In cases with gravitational waves, the differences are more substantial. Most notably,  $\rho$  and  $\rho'$  are constant in all cases. This can be seen from the linearized equation - substituting in the initial conditions of  $\rho = \sqrt{-\Lambda}$  and  $F = \bar{F} = -3\sqrt{-\Lambda}$  into equation 3.7 for  $\partial_t\rho$  it can be seen that  $\partial_t\rho$  will be zero initially, and since  $\rho$  hence will not change, and noting that  $F$  and  $\bar{F}$  are defined as constant by the gauge, it follows that  $\rho$  is constant at all times in the linear case, and the same can be likewise proven for  $\rho'$ . All the changes in  $\rho$  and  $\rho'$  are thus non-linear effects, with the relevant terms causing this effect being  $\sigma\bar{\sigma}$  for  $\rho$  (equation 2.16) and  $\sigma'\bar{\sigma}'$  for  $\rho'$  (equation 2.17). Similarly,  $\mu$  is constant at zero in all linear cases, and  $H$  too is unaffected by the waves. However, many effects are similar in the linear case to the non-linear - the  $\psi_4$  wave grows as it travels whereas the  $\psi_0$  wave shrinks as in the non-linear case,  $\sigma$  and  $\sigma'$  increase or decrease in the same way as the wave passes, and collision and post-collision effects are similar.

# Chapter 5

## Conclusion

In this project, a numerical simulation developed in COFFEE for plane-symmetric gravitational waves, using the Newman-Penrose formalism, was applied to anti-de Sitter space-time. The use of this simulation was justified by a convergence test, which showed the simulation correctly converged such that the constraint quantities tended towards zero as the number of grid points was increased. The most notable feature found about AdS was the asymmetry between waves travelling in the two possible directions with, for instance,  $\psi_4$  waves growing in amplitude as they travel and  $\psi_0$  waves decreasing, unlike in de Sitter space-time where both grow at the same rate and Minkowski space-time where neither change in amplitude, and follow-on effects such as an asymmetric growth of  $I$  after a collision between initially identical waves, whereas in the other two space-times the growth is symmetrical. This was found to be a result of the initial conditions for AdS, in which  $\rho$ , which affects the growth of  $\psi_4$ , starts positive and  $\rho'$ , which affects the growth of  $\psi_0$ , starts negative, an asymmetry which is not present in the other space-times. Simulation runs with linearized evolution equations showed many effects, such as waves indirectly causing changes in  $\rho$  and  $\rho'$ , to be only relevant in the non-linear domain, however, the asymmetric growing and shrinking of gravitational waves was shown to hold even in the linear case. For future research, an important aspect of the subject not covered in this report is, as can be seen by the shape of the contour plots (see, eg. Figure 4.4), that the time-like surfaces in AdS become null-like after some period of time, causing the simulation to break down (this happens more rapidly for larger negative cosmological constants). It may also be beneficial to explore the effects of more complex wave-forms, to see if any further interesting features of AdS can be ascertained.

# Chapter 6

## References

- Bengtsson, I. (1998). Anti-de Sitter Space.
- Carpenter, M. H., Gottlieb, D., & Abarbanel, S. (1994). Time-stable boundary conditions for finite-difference schemes solving hyperbolic systems: Methodology and application to high-order Compact Schemes. *Journal of Computational Physics*, 111(2), 220–236. <https://doi.org/10.1006/jcph.1994.1057>
- Doulis, G., Frauendiener, J., Stevens, C., & Whale, B. (2019). Coffee—an MPI-parallelized python package for the numerical evolution of differential equations. *SoftwareX*, 10. <https://doi.org/10.1016/j.softx.2019.100283>
- Frauendiener, J., & Stevens, C. (2014). Numerical evolution of plane gravitational waves in the Friedrich-Nagy gauge. *Physical Review D*, 89(10). <https://doi.org/10.1103/physrevd.89.104026>
- Frauendiener, J., Hakata, J., & Stevens, C. (2021). Can gravitational waves halt the expansion of the universe? *Universe*, 7(7). <https://doi.org/10.3390/universe7070228>
- Friedrich, H., & Nagy, G. (1999). The initial boundary value problem for Einstein’s vacuum field equation. *Communications in Mathematical Physics*, 201(3), 619–655. <https://doi.org/10.1007/s002200050571>
- Griffiths, J. B. (2016). Colliding plane waves in general relativity. Dover Publications, Inc.
- Hawking, S. W., & Ellis, G. F. R. (1973). The large scale structure of space-time. Cambridge University Press.
- Hubeny, V. E. (2015). The ADS/CFT correspondence. *Classical and Quantum Gravity*, 32(12). <https://doi.org/10.1088/0264-9381/32/12/124010>
- Newman, E., & Penrose, R. (1962). An approach to gravitational radiation by a method of spin coefficients. *Journal of Mathematical Physics*, 3(3), 566–578. <https://doi.org/10.1063/1.1724257>
- Penrose, R., & Rindler, W. (1986). Spinors and space-time (Vol. 1). Cambridge University Press.
- Strand, B. (1994). Summation by parts for finite difference approximations for  $D/DX$ . *Journal of Computational Physics*, 110(1), 47–67. <https://doi.org/10.1006/jcph.1994.1005>